



Unique Radar Observations of Large Raindrops in Tropical Warm Rain during PISTON

KYLE CHUDLER,^a STEVEN A. RUTLEDGE,^a AND BRENDA DOLAN^a

^a *Department of Atmospheric Science, Colorado State University, Fort Collins, Colorado*

(Manuscript received 11 November 2021, in final form 27 June 2022)

ABSTRACT: Isolated warm-rain cells are an important feature over the tropical oceans. Although warm rain is typically associated with relatively small raindrops, large raindrops (>4.5 mm in diameter) have been observed in some cases. Previous studies have examined warm rain cells with large drops on a case-study basis, but they have yet to be investigated in a broader, statistical sense. During the recent Propagation of Intraseasonal Oscillations (PISTON) field campaign, a C-band polarimetric radar routinely measured extreme values of differential reflectivity in small, isolated convection, indicating the presence of large drops. Using an objective feature identification and tracking algorithm, this study offers new insights to the structure and frequency of cells containing large drops. Cells with high differential reflectivity (>3.5 dB) were present in 24% of all radar scans. The cells were typically small (8-km² mean area), short lived (usually <10 min), and shallow (3.7-km mean height). High differential reflectivity was more often found on the upwind side of the cells, suggesting a size sorting mechanism was operating establishing a low concentration of large drops on the upwind side. Differential reflectivity also tended to increase at lower altitudes, which is hypothesized to be due to continued drop growth and increasing temperature (increasing the dielectric constant of water). Rapid vertical cross-section radar scans, as well as transects made by a Learjet aircraft with onboard particle probes, are also used to analyze these cells, and support the conclusions drawn from statistical analysis.

KEYWORDS: Tropics; Precipitation; Cloud microphysics; Radars/Radar observations

1. Introduction and background

a. Tropical warm rain

Over the tropical oceans, isolated raining cells, including some with tops near the freezing level, are ubiquitous. These warm rain convective cells, defined as clouds which produce precipitation from condensation and collision-coalescence, are an important feature over the warm oceans (Johnson et al. 1999; Lau and Wu 2003). Previous studies have found that between 10% and 30% of all precipitation in the tropics falls as warm rain, depending on the method used to identify warm rain cells (Rickenbach and Rutledge 1998; Johnson et al. 1999; Petty 1999; Stephens et al. 2002; Lau and Wu 2003; Schumacher et al. 2007). In addition to this precipitation contribution, warm rain cells have also been shown to have significant impacts on heating profiles. During the Tropical Ocean and Global Atmosphere Coupled Ocean-Atmosphere Response Experiment (TOGA COARE), Schumacher et al. (2007) observed several periods with enhanced low-level heating and attributed these periods to latent heating owing to the presence of cumulus congestus clouds. The large albedo of

these clouds (compared to the dark ocean below) also has significant impacts on radiative forcing (Hartmann and Short 1980; Slingo 1990). In Johnson et al. (1999), a trimodal structure of tropical convection was demonstrated, wherein cumulus congestus served as an intermediary between shallow fair-weather (including non-precipitating) cumulus and deep cumulonimbus-producing convection. These congestus clouds, which were argued to be primarily associated with warm rain processes, act to moisten the midlevels of the atmosphere, which is an important precursor to deep convection. It is clear that this shallow to moderate depth convection, producing precipitation through primarily warm-rain processes has important feedbacks to latent heating and energetics, the water cycle, and the broader tropical environment.

An interesting phenomenon which has previously been observed in the tropics is the presence of large (>4.5 mm) raindrops in warm rain cells (Beard et al. 1986; Rauber et al. 1991; Takahashi et al. 1995; Szumowski et al. 1997, 1998, 1999; Hobbs and Rangno 2004; Gatlin et al. 2015). Drops of this size are common in the midlatitudes where melting hail routinely leads to large drops. However, in the tropics, drop sizes are typically smaller (median drop diameter $D_0 < 1$ mm; Bringi et al. 2003; Ulbrich and Atlas 2007; Bringi et al. 2009; Thurai et al. 2010; Thompson et al. 2015; Dolan et al. 2018), so the presence of large drops is more remarkable. Moreover,

Corresponding author: Kyle Chudler, kyle.chudler@colostate.edu

previous studies (Beard et al. 1986; Rauber et al. 1991; Szumowski et al. 1997, 1998, 1999) have observed large drops in cells confined to at or below the melting level (~ 5 km), making it impossible for ice to contribute to the production of large drops.

In their extensive work cataloging over 9000 h of disdrometer data from across the globe, Gatlin et al. (2015) found, perhaps surprisingly, that large raindrops were actually more commonly found at tropical locations than subtropical or high-latitude locations. However, the vertical extent of the clouds (i.e., whether they were above the freezing altitude or not) was not considered, so, as was stated in the study, a substantial portion of these large drops likely formed from melting hail and graupel rather than warm rain. In the Joint Hawaiian Warm Rain Project (JHWRP), drops were observed in warm rain clouds off the coast of Hawaii that often exceeded 4 mm in diameter, with a maximum diameter of 8 mm (Beard et al. 1986; Rauber et al. 1991). Using aircraft disdrometer data and simple collection equations for raindrop growth, Beard et al. (1986) suggested that the high liquid water content in the region, combined with strong updrafts ($\sim 7\text{--}10$ m s $^{-1}$), was sufficient to explain the formation of the large drops. Rauber et al. (1991) proposed a different mechanism for large drop formation, wherein raindrops circulated between the updraft and downdraft of a convective cloud, allowing extended periods of accretional growth of these drops with small cloud droplets. As the updraft weakened, the large drops then fell through the former updraft channel where smaller drops, which would have otherwise caused collisional breakup of the large drops, were largely absent. However, these “clean” updraft channels likely still contain a high concentration of very small cloud drops, which are continuously forming, and promote further drop growth without being large enough to cause breakup.

Building on the JHWRP, the Hawaiian Warm Rain Project (HaRP) further investigated the warm rain processes leading to large drops. Szumowski et al. (1997, 1998, 1999) explored the formation of these large drops. They found that, within a window as short as 15 min, shallow cells with intense updrafts ($5\text{--}9$ m s $^{-1}$) could produce drops as large as 8.5 mm in diameter. The formation of large drops was favored in low wind shear environments, where updrafts were not tilted significantly. In these cases, drops would remain suspended above or within the updraft, where liquid water content was high, and drops could grow rapidly. Furthermore, these updraft channels were also hypothesized to be relatively clear of smaller raindrops. This is possibly due to a sedimentation size-sorting mechanism, where large drops fall through the updraft while smaller ones are suspended aloft (i.e., Kumjian and Ryzhkov 2012), resulting in a “clean” channel for large drops to fall through, and lowering the likelihood of collisional breakup with smaller drops. In the sheared/tilted updraft case, large drops are deposited away from this “clean” updraft channel and may be prone to breakup induced by collisions with smaller drops. This is consistent with part of the mechanism put forth by Rauber et al. (1991). During HaRP, they also found the large nucleating aerosols, such as those provided by sea spray, were precursors to large drop

formation, providing a relatively large starting point for droplets to grow.

b. PISTON observations

The Propagation of Intraseasonal Oscillations (PISTON) Field Campaign, which took place in the open waters of the western North Pacific during the late summer and early autumn of 2018 and 2019 (Sobel et al. 2021), provided an opportunity to observe warm rain cells (along with other types of oceanic convection) in detail. On board the R/V *Thomas G. Thompson* (in 2018) and R/V *Sally Ride* (in 2019) was the Colorado State University SEA-POL radar (Rutledge et al. 2019a,b), a polarimetric weather radar which took measurements of precipitation for the duration of both cruises. Using data from SEA-POL, Chudler and Rutledge (2021) found that small, isolated convection (primarily composed of warm rain cells) were present in over 90% of the SEA-POL scans and contributed 11% of the radar-measured rain volume.

An interesting feature which was frequently noted during PISTON was the tendency for isolated convection to contain small areas with extremely high values of differential reflectivity. An example of this phenomenon is shown in Fig. 1. Differential reflectivity (Z_{DR}), defined as the logarithm ratio of the horizontally and vertically polarized radar reflectivities, provides a measurement of the reflectivity-weighted oblateness of drops within a radar volume, with positive values corresponding to drops which have a larger horizontal axis in comparison to the vertical axis. While small raindrops (<1 mm in diameter) are nearly spherical ($Z_{DR} \approx 0$ dB), larger drops are distorted into oblate shapes (Pruppacher and Klett 1978), thus increasing Z_{DR} . During PISTON, cells with Z_{DR} in excess of 3.5 dB were frequently observed, and occasionally reached 7 dB or higher. The relationship between drop size and Z_{DR} for a 5.65-GHz radar (identical to SEA-POL's) is shown in Fig. 2. The calculations for a 3-GHz S-Band radar are also plotted for comparison. For drop diameters below ~ 4.5 mm ($Z_{DR} < 3.5$ dB), in the Rayleigh scattering regime, Z_{DR} increases approximately linearly with drop size. Past this point, however, as drop size enters the Mie scattering regime for the 5.6-GHz radar (5-cm wavelength), a prominent spike in Z_{DR} is evident, caused by resonance effects (Bringi et al. 1991; Zrnić et al. 2000; Carey and Petersen 2015). This Mie scattering artifact makes the extreme Z_{DR} values observed in rain more readily explainable, as values of over 7 dB would be highly unlikely in a Rayleigh scattering regime (with the exception of insects, whose size and large shape asymmetries could cause extreme Z_{DR} , but are unlikely to be found over the open ocean). However, even after accounting for Mie scattering, Z_{DR} values of over 3.5 dB still suggest drop sizes in excess of 4.5 mm, which again is a curious feature in tropical warm rain cells. The region between 4.5 and 6.75 mm in Fig. 2 is referred to as the “resonance zone,” marking where Mie effects lead to a nonlinear increase in Z_{DR} , and in fact in this region, Z_{DR} -based estimates of the drop size are ambiguous. The beginning of this resonance zone (3.5-dB Z_{DR} /4.5-mm drop size) will serve as a general threshold for large drops in this study, although it is noted that the monodisperse drop size

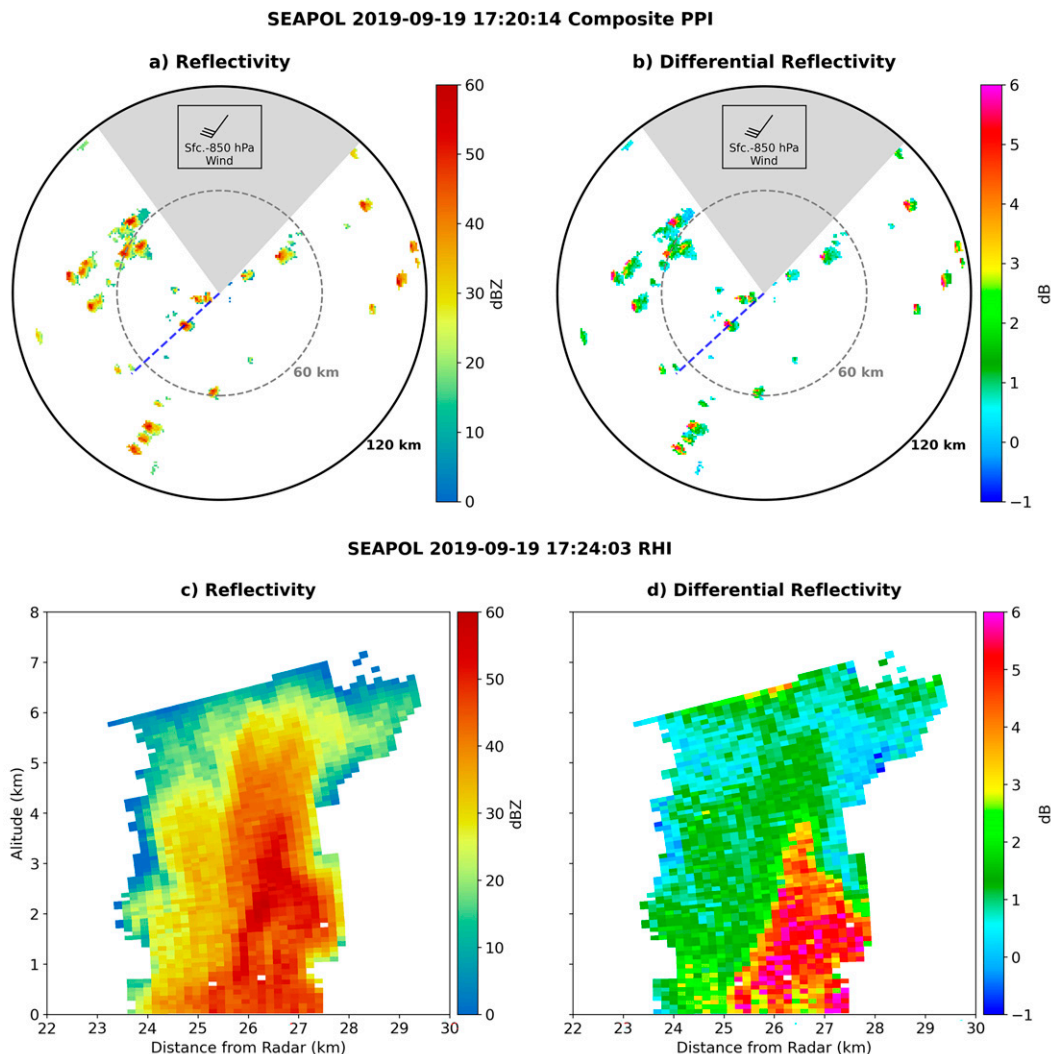


FIG. 1. Example of cells with high Z_{DR} seen by SEA-POL. PPI images of top-down views of (a) reflectivity and (b) differential reflectivity, and (c),(d) RHI images show vertical cross sections of the same variables. The location of the cross section plotted in the RHI images in (c) and (d) is marked with a blue dotted line in the PPIs in (a) and (b). The mean surface–850-hPa wind vector is shown in (a) and (b), as determined from the radiosonde launch occurring closest to the SEA-POL scan time.

used to create Fig. 2 is not necessarily representative of the true drop size distribution of these cells. However, even in a more realistic drop size distribution, it is expected that a 3.5-dB Z_{DR} signature would require at least *some* large drops to be present, so it is still used as a convenient threshold here. Thus, a diameter of 4.5 mm will serve as a general threshold for large drops in this study.

Although studies on large drops forming in warm rain are sparse (notably only from the JHWRP and HaRP studies discussed above), it appears that given the right conditions (i.e., high liquid water content, strong and upright updrafts, and large nucleating aerosols), large drops can form through warm rain processes alone, without the need for melting ice. While these studies outlined the possible mechanisms for large drop growth, they lack in continuous robust

observations, which the present study seeks to build upon. First, the JHWRP and HaRP studies are based primarily on analysis of a few case studies. With over 7000 volume scans collected during ~ 70 days at sea, the SEA-POL dataset allows for a robust statistical analysis of the characteristics of these large drop-producing storms. Additionally, while Szumowski et al. (1997, 1998, 1999) also utilized a C-band radar in their analysis, it was a single-polarized radar, and subsequently only reflectivity and radial velocity were examined. The polarimetric products offered by SEA-POL, particularly Z_{DR} , provide a more direct measurement of drop size and shape, which is of central importance to this analysis. This study seeks to leverage the high-resolution and long-term polarimetric observations from SEA-POL to characterize warm rain cells, particularly those which develop regions of high

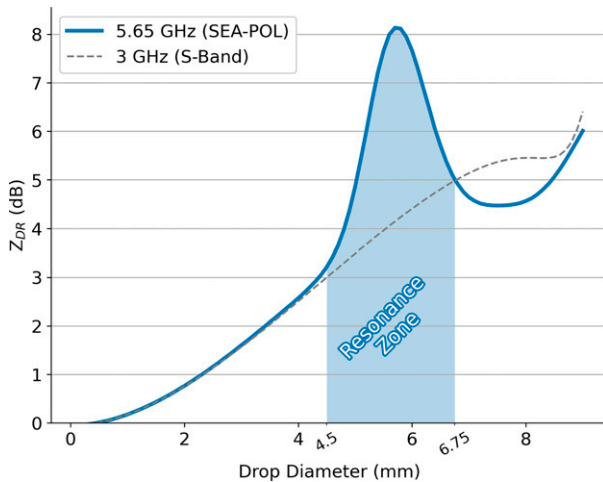


FIG. 2. Simulated Z_{DR} vs drop diameter for SEA-POL (5.65 GHz, blue line) and a 3-GHz radar (dashed gray line). A “resonance zone” is marked between 4.5 and 6.75 mm, where Mie scattering effects lead to increased Z_{DR} . Scattering parameters are detailed in section 2c.

(magnitude) Z_{DR} values. In addition to the polarimetric radar data, several other techniques and datasets are used, including scattering simulations, numerical drop growth modeling, and aircraft particle probe measurements. By combining these diverse datasets and methods, this study provides a detailed investigation into the processes leading to large drop formation in warm rain cells.

This paper will be organized as follows. First, section 2 will provide an overview of the SEA-POL radar scanning strategies, and the methods used to quality-check and process the data. Section 2 also reviews the methods used for scattering calculations and drop growth simulations, as well as provide some detail on the other data sources used in this study. Section 3 showcases two examples of high Z_{DR} values observed in isolated warm rain cells—one observed by aircraft transects, and one observed with rapid vertical cross sections from SEA-POL. Section 4 then provides a more detailed analysis of isolated cells with high Z_{DR} , examining their frequency, structure, and possible methods for formation of large drops based on polarimetric analysis, scattering simulations, and a simple drop growth model. Finally, these results are synthesized and summarized in section 5.

2. Data and methods

a. SEA-POL radar

The radar data used herein were collected by the Colorado State University SEA-POL radar, a polarimetric C-band weather radar designed for use at sea. This work primarily uses the 360° plan position indicator (PPI) volume scans, which were taken every 15 min in 2018 and every 10 min in 2019. The exact elevation angles used in the volume scans depended on the scanning strategy being used at the time (which was determined based on the proximity and height of

precipitation around the radar). The lowest angle used in a PPI scan was typically 0.5° or 0.8°. These PPI scans were then interpolated onto a regular 300 km × 300 km × 15 km (x - y - z) grid, with grid spacings of 1 km in the horizontal and 0.5 km in the vertical. Although this gridding did lead to some smoothing out of the true peak values of Z_{DR} (a main focus of this study), the final grid resolution is high enough that this is not expected to be significant. Convective/stratiform partitioning using the texture-based Steiner et al. (1995) and rain rate following the Thompson et al. (2018) methodology for tropical rain (based on drop-size distributions collected from a disdrometer dataset) were calculated at each grid point. In addition to the PPI scans, range height indicator (RHI) scans were performed in-between PPI scans, which are examined for a case study presented in this paper. These RHI scans provide vertical cross-section “slices” of echoes at high spatial resolution. During the 2019 operations, rapid RHI scans were the focus, with sweeps being separated by as little as 15 s. The storm target for the RHI scans was chosen at the discretion of the radar operator. Note that, unlike the PPI data, the RHI scans were not gridded and have been left in their native spherical coordinates. Also utilized in 2019 was a scanning strategy which was optimized for rainfall mapping. As this scanning strategy focuses on capturing the lower levels of storms, storms were occasionally not topped by the radar beam, and their vertical extents therefore not fully captured. Thus, data on the vertical structure of storms from PPI scans is more limited for 2019. A more detailed explanation of the scanning strategies employed during PISTON, as well as the rigorous quality-control process used on the data, can be found in Chudler and Rutledge (2021).

While polarimetric radar retrievals from SEA-POL could theoretically be used to compute drop size distribution parameters (e.g., Brandes et al. 2004), which would seemingly be a useful tool for this study looking at large drops, such analysis was not done in the present study. The focus of this study is on the large drop regime, where Mie effects introduce nonlinearities which convolute drop size distribution (DSD) retrievals. While we could limit the retrievals to points outside of the Mie regime, this would preclude the regions we are most specifically trying to understand. Furthermore, while a hydrometeor identification algorithm could be used to detect large drops, such an algorithm would likely primarily use Z_{DR} to detect large drops, and therefore would not provide any additional information beyond what can be gleaned by looking at individual radar variables.

b. Feature detection and tracking

To identify and analyze the warm rain cells, the precipitation feature identification method outlined in Chudler and Rutledge (2021) was utilized. This method identifies and groups contiguous regions of reflectivity pixels greater than a specified threshold (17 dBZ), and then attributes each of these “features” with statistics such as echo top height, maximum/mean reflectivity and rain rate, total area, etc. For the 2019 data, echo top heights were only calculated for storms

that had their full vertical extent captured by SEA-POL (see note in section 2a). For the present study only “isolated” features (those with a maximum horizontal dimension of less than 20 km) are examined (sub-MCS and MCS features are grouped into a single “non-isolated” category, and linearity is not considered). Additionally, while Chudler and Rutledge (2021) used the 2-km grid level to identify and group features, the present study groups features based on composite reflectivity, or the maximum reflectivity observed throughout the vertical column at each horizontal grid point. This is done in order to align with the methods employed by the cell-tracking algorithm discussed in the subsequent paragraph. Sensitivity tests show that the overall feature statistics do not change significantly between using 2 km and composite reflectivity for identifying features, with a modest increase in average feature area being the most notable change.

While the feature identification method described above provides a method for identifying features in each SEA-POL scan, it has no way of deriving temporal continuity of features between scans. That is to say, a single cell which in reality persists between SEA-POL scans as a single entity will be identified as two separate features by the Chudler and Rutledge (2021) method. To glean information on the statistics of these cells throughout their lifetime, a different algorithm is desired. Toward that end, the Thunderstorm Identification, Tracking, Analysis, and Nowcasting (TITAN) cell tracking technique (Dixon and Wiener 1993) is utilized in the present study. Specifically, the TINT Python package (<https://github.com/openradar/TINT>) developed by Fridlind et al. (2019), which takes the TITAN algorithm and wraps it up into a convenient and computationally efficient Python program, is used for analysis herein. As modified for the present study, this algorithm takes two successive SEA-POL scans at time t_0 and t_1 , identifies the features in each scan based on the Chudler and Rutledge (2021) method (i.e., a contiguous region of 2-km reflectivity pixels > 17 dBZ), and then attempts to pair features together between t_0 and t_1 based on phase correlation calculations for each feature, while also taking into account the previous motion of the feature. While the TINT package does provide a limited set of attributes of each feature in addition to tracking them, more detailed statistics were desired. Accordingly, the modified Chudler and Rutledge (2021) feature identification/characterizing code was merged with the TINT algorithm for this study, resulting in a robust database which provides the track and attributes of all features seen by SEA-POL throughout their lifetimes.

In addition to identifying and tracking raining features, a separate routine was run to track and identify high Z_{DR} cores (HZCs) within convective cells in PPI scans. An HZC is defined as a cluster of Z_{DR} pixels within an isolated cell which is made up of at least five contiguous pixels of composite $Z_{DR} > 3.5$ dB at an altitude of 2 km. The five-pixel threshold was chosen to exclude spurious noise and nonmeteorological sea clutter which occasionally led to very small regions of high Z_{DR} . The 3.5-dB Z_{DR} threshold was chosen as it is the approximate threshold at which Mie scattering effects commence, and is associated with drop diameters of ~ 4.5 mm (see Fig. 2). It should be noted that although there is a sudden

jump in Z_{DR} around this diameter, this is due to the specific frequency (5.65 GHz) used by the SEA-POL radar, and has no particular physical significance in terms of drop size. Echoes on either side of this Mie scattering threshold may have drastically different Z_{DR} values; however, their drop sizes may be relatively similar. Additionally, the 3.5-dB threshold arose from a monodisperse drop distribution assumption, which may not be entirely realistic. The 3.5-dB threshold is somewhat arbitrary in that regard; however, it still serves as convenient marker for defining a cell that contains large drops. By definition, HZCs are considered subfeatures of larger, parent cells. Essentially, each larger parent feature was marked at each time step as either having an embedded HZC or not, depending on if the Z_{DR} pixels within it met the parameters above. For large and moderately sized features, it is possible (and in fact sometimes observed) that multiple HZCs could be contained within one parent feature, which was not directly considered in this study. Additionally, the TINT algorithm was only used to track the parent cells, not the HZCs themselves. It is assumed that if a TINT-tracked isolated cell persists from one scan to the next, and that an HZC is present in both, that this HZC is a single, persistent entity. HZCs were only identified in PPI scans (not RHIs).

The relative location of HZC cells within their parent cells is also examined in this study. For this analysis, the upwind/downwind “edge” of a cell was defined as the furthest upwind/downwind point from the cell center with a reflectivity greater than or equal to 17 dBZ (the same threshold used for feature identification). Wind direction was determined from the sounding which was launched nearest to the time the cell was observed. Each vertical radar grid level was considered independently and matched to the wind direction at the closest vertical sounding level. As previous studies have noted, it is more realistic to use storm-relative wind direction than environmental wind when addressing questions of size sorting (Kumjian and Ryzhkov 2012; Dawson et al. 2015; Loeffler and Kumjian 2020). Toward that end, the environmental sounding wind was combined with cell motion based on the tracking algorithm to arrive at a storm-relative wind direction, which was used for subsequent upwind/downwind calculations. These studies also suggest that size sorting occurs above the level where the radar signal is actually seen. However, in most HZC cases, 0–5-km wind shear was relatively low (~ 13 kt; 1 kt ≈ 0.51 m s $^{-1}$), and sensitivity tests suggest that choosing a higher altitude to select wind direction did not significantly impact results.

1) SCATTERING AND DROP GROWTH SIMULATIONS

In addition to using polarimetric radars such as SEA-POL to examine the Z_{DR} of observed storms, Z_{DR} can also be numerically simulated for any given distribution of drop sizes, using T-matrix scattering simulations (Mishchenko et al. 1996). In this study, this capability is leveraged to further explore the microphysical properties of shallow convection. Simulations were conducted at 5.67 GHz with a mean canting angle of 0° and a standard deviation of 10° , and an assumed drop-shape relationship given in Beard and Chuang (1987).

Unless otherwise indicated, the temperature was set to 20°C. Monodisperse simulations used a concentration of $10 \text{ m}^{-3} \text{ mm}^{-1}$, although we note that this does not impact the resulting Z_{DR} values. By examining the simulated Z_{DR} of various hypothetical drop size distributions, the spatial patterns of Z_{DR} observed in real SEA-POL data can be more readily explained, and a more cohesive framework for formation of large drops can be developed.

We also undertook several sensitivity studies relative to the DSD that could influence Z_{DR} values. For these calculations, two years of data from the two-dimensional video disdrometer located at the U.S. Department of Energy Atmospheric Radiation Measurement Program site on Manus Island, Papua New Guinea, were used to create a baseline “small drop” concentration (Thompson et al. 2015). To represent the typical drop size distribution which may be associated with convective cells, all record times which logged a rain rate of $>10 \text{ mm h}^{-1}$ and a Z_{DR} of $<2 \text{ dB}$ were averaged into a single distribution. This baseline distribution was then multiplied by various concentration factors from 0 (no small drops used) to 1 (entire small drop concentration used), and “mixed” with 5-mm drops with a fixed concentration of $5 \text{ m}^{-3} \text{ mm}^{-1}$. This large drop size and concentration was chosen to be consistent with the concentration and size of large drops found in the HaRP project (Szumowski et al. 1997, 1998, 1999), and also agree with the findings of in situ aircraft disdrometer measurements from PISTON (see section 3a). The polarimetric moments for these different DSD were calculated using the PyDSD software package (<https://github.com/josephardinec/PyDSD>) with the scattering parameters described above.

In addition to scattering simulations, this study also makes use of a theoretical drop growth equation to investigate the growth of rain drops in tropical convection under different microphysical parameters. As has been done in previous studies (Beard et al. 1986; Szumowski et al. 1997, 1998, 1999), a simple continuous collection equation will be used to simulate droplet growth:

$$\frac{dr}{dt} = \frac{V_r W_l E_c}{4\rho_l},$$

where V_r is droplet fall speed, W_l is liquid water content, E_c is collision efficiency, and ρ_l is the density of water. The droplet fall speed V_r is derived from the Gunn and Kinzer (1949) droplet terminal velocity experiments, and E_c is from Yau and Rogers (1996, Table 8.2). Drop growth calculations were performed with a time step of 30 s and continued until the droplet dropped below the height they were released at, representing the cloud base. By using this drop growth equation, the conditions under which large drops can rapidly form are examined and compared to the conditions observed during the PISTON cruise (see section 4d). While a more complex model which takes into account size sorting and collisional breakup would perhaps lead to more accurate results, developing such a model was beyond the scope of this study, and was found to be unnecessary to produce large drops. Furthermore, under the Rauber et al. (1991) “clean” updraft hypothesis, large drops can necessarily only form when collisional

breakup is not an issue, so including that process in the model may be unnecessary.

2) AIRCRAFT PARTICLE PROBE

During the 2019 PISTON campaign, collaborative operations were occasionally run with the Cloud, Aerosol and Monsoon Processes Philippines Experiment (CAMP²Ex, <https://camp2ex.jpl.nasa.gov>) project, which was ongoing in the same region that year. The CAMP²Ex field project involved multiple aircraft, including the SPEC Inc. Learjet, which was outfitted with a suite of state-of-the-art particle probes (Lawson et al. 2015) capable of taking measurements of cloud/rain drop sizes and concentrations across a wide spectrum, including a fast forward scattering spectrometer probe, a fast cloud droplet probe (FCDP), a high volume precipitation probe (HVPP), a 2D-S probe and a Hawkeye probe. These in situ measurements are extremely valuable, as they can provide confirmation of the drop size properties being inferred from SEA-POL polarimetric measurements. On 10 September, a shallow convective cell with high Z_{DR} was measured by both the SEA-POL radar and the Learjet particle probes. This case is examined in detail in section 3a. The DSD for this case was synthesized from the FCDP, HVPP, and 2D-S probes, and were integrated over a 5-s span during the pass.

3) RADIOSONDES

Sounding data used in this study comes from Vaisala RS41-SGP radiosondes, which were launched every 3 h from the PISTON ships. Sounding data were interpolated to regular 5-hPa intervals and quality controlled according to Ciesielski et al. (2014).

3. Case studies

a. Learjet observations

On September 10, the concurrent measurements of an isolated cell with HZC were made with both the SEA-POL radar and the Learjet particle probes (Fig. 3). Although the cell was short-lived ($<30 \text{ min}$), the Learjet was able to make two passes through the upper and lower portions of the cell. Figure 3 shows a vertical cross section of the cell which was captured by SEA-POL near the time of the passes.

The drop size distributions recorded by the Learjet probes during each pass are shown in Fig. 4. During the first pass through the upper portion of the storm, where Z_{DR} was 3–4 dB, the Learjet recorded drops up to 3.75 mm in diameter. This pass featured a very high liquid water content (LWC) over 2 g m^{-3} , in part due to a very high concentration of small 10–50- μm cloud droplets. Szumowski et al. (1999) suggested that drop growth is most rapid in the near-suspension and early-fall period near the top of the cloud, which is certainly plausible in this case given the very high liquid water content. Approximately 3 min later, the aircraft made a pass through a rain shaft below cloud base. Here, drops up to 4.5 mm in diameter were observed. This increase in drop size corresponds with an increase in Z_{DR} seen by SEA-POL (Fig. 3b), with values over 5.5 dB

SEAPOL 2019-09-10 02:13:25 RHI

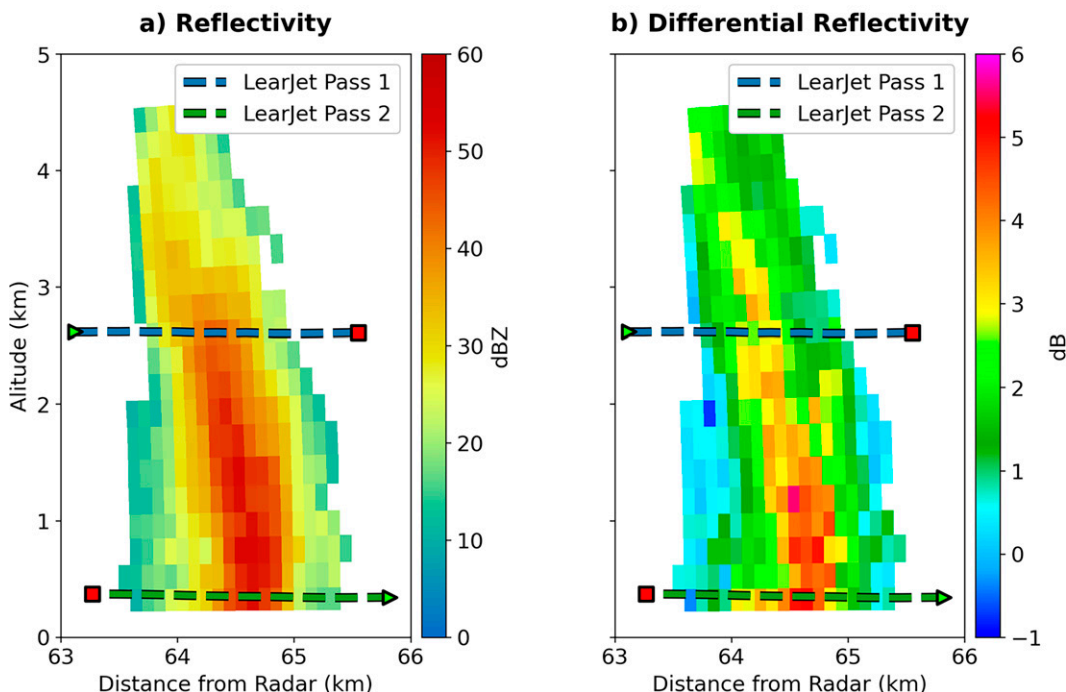


FIG. 3. Vertical cross section of an HZC cell sampled by the Learjet aircraft. The dashed lines mark the path of the Learjet, which made two passes through the storm. The upper pass (blue) occurred at 0213 UTC, and the lower pass (green) occurred at 0216 UTC. The green triangle and red square markers denote the beginning and ends of the passes, respectively.

measured near the lowest portion of the scan. This apparent increase in drop size at lower elevations will be a focus of later sections.

b. Rapid vertical cross-section scans

During PISTON 2019 operations, focus was placed on capturing the vertical evolution of storms at a high temporal resolution. Toward that end, rapid vertical cross sections were obtained between horizontal scans. With this scanning method, high-resolution vertical cross sections of storms

could be captured as frequently as once every 15–30 s. In practice, the rapid formation and decay of isolated cells, along with the motion of the ship, proved to make capturing the evolution of an HZC quite difficult. However, on days where storm motion was very slow and the ship was stationary, this task was feasible. The following section examines the evolution of one HZC cell on which rapid vertical scans were successfully obtained.

On 22 September 2019, rapid successive vertical cross sections were taken of a small, isolated cell near SEA-POL (Fig. 5). This cell was very small—approximately 1 km wide and only 3 km in

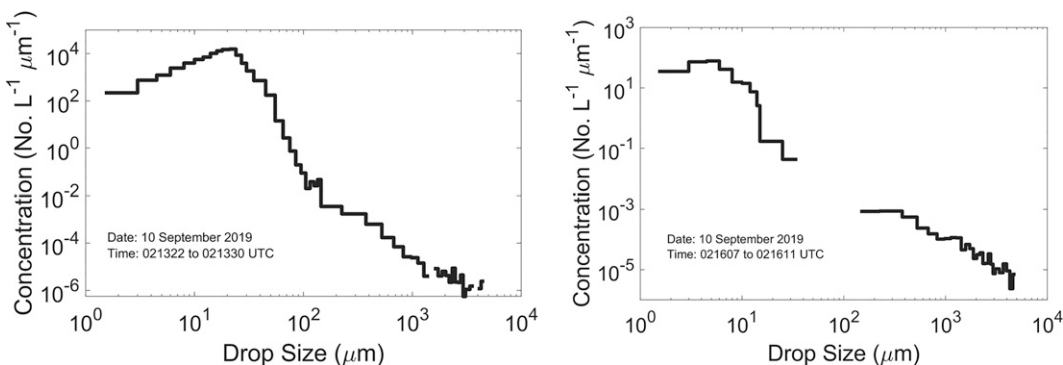


FIG. 4. Drop size distribution measured by the Learjet particle probe during the flight paths drawn in Fig. 3. Data in the left panel and right panels correspond with the upper and lower passes marked in Fig. 3, respectively.

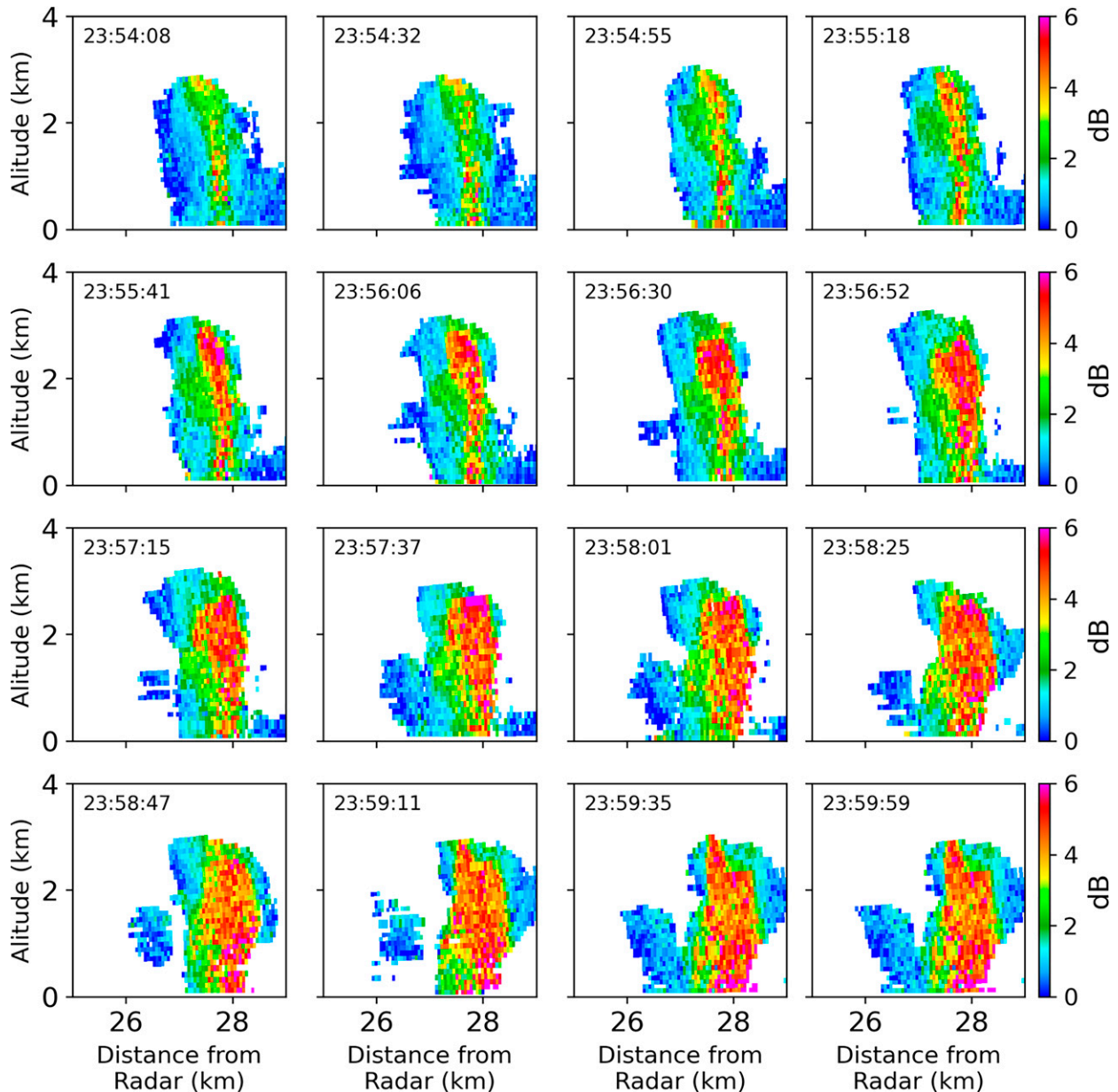


FIG. 5. Vertical cross sections of Z_{DR} showing the evolution of an HZC cell, captured using rapid vertical cross-section scans from the SEA-POL radar. The timestamp in the upper-left corner of each plot marks the start time of each scan.

height. Despite its diminutive size, at its peak SEA-POL observed a reflectivity of 57 dBZ and Z_{DR} in excess of 10 dB. It is worth recalling here that the relationship between drop size and Z_{DR} is nonlinear, and that higher Z_{DR} does not necessarily mean larger drops are present. In fact, beyond a drop diameter of around 5.7 mm, Z_{DR} actually begins to decrease (see Fig. 2). Rather, the Z_{DR} response is greatest in a “resonance zone” between ~4.5–6.75 mm, and an increase in Z_{DR} should be interpreted as an increase in the concentration of drops in this size range, or a decrease in the concentration or smaller drops which would otherwise have a masking effect (see section 4c).

At the time of the first scan (2354:08 UTC, top left of Fig. 5), an HZC had already begun to form, with a very narrow (~300 m) channel of 2–4-dB Z_{DR} , presumably corresponding to the location of the updraft. As time progressed, Z_{DR} increased, with the largest Z_{DR} values appearing at the top of the cell first. By 2355:41 UTC, Z_{DR} values up to 6 dB were located at the top of the cell, while Z_{DR} in the remainder of the column was still primarily in the 3–4-dB range. This Z_{DR} maximum at cell top then began to cascade downward, as well as expand horizontally. By 2358:47 UTC, the large Z_{DR} values reached the surface,

including values in excess of 10 dB. Overall, these snapshots demonstrate a scenario in which drops undergo rapid growth at the top of the updraft (Z_{DR} increasing from 3 to 6 dB in ~ 90 s). The large drops could then no longer be supported by the updraft (either due to their increase in mass or a decrease in updraft intensity, or both), and began to fall toward the surface. As they fell, Z_{DR} continue to increase, likely due to some combination of continued coalescence and temperature effects (Zrnić et al. 2000, see section 4c). Near the surface, Z_{DR} exceeded 10 dB at a few localized points, suggesting radar volumes which were composed primarily of very warm (25°C , the approximate wet bulb temperature) drops in the Mie resonance range (4.5–6.75 mm), with few or no small drops.

This vertical evolution of Z_{DR} values is also represented in Fig. 6, which depicts the 90th percentile of Z_{DR} values at each level for each scan in Fig. 5. Initially, Z_{DR} is close to uniform throughout the column, with values generally between 2 and 3 dB. As time progresses, Z_{DR} increases throughout the column, but with the largest increase near cell top, where values up to 5–6 dB begin to appear, and decreasing to 3–4 dB near the surface. At the end of the scanning period, Z_{DR} remains very high at cell top (5 dB), but the largest Z_{DR} values are found near the surface (5–7 dB). Again, this demonstrates a Z_{DR} signal which is influenced by multiple factors—drops that grow rapidly aloft and continue to grow as they fall, and increasing resonance/Mie effects as temperature increases with decreasing altitude.

4. Statistical results

a. General statistics

The following section will discuss the general attributes of HZCs and the convective cells that contain them. Approximately one-quarter (24%) of the SEA-POL scans contained at least one HZC echo. Although on an individual basis isolated cells actually only rarely developed an HZC (2% of all isolated cells), the ubiquitous nature of isolated cells resulted in HZCs being present a significant portion of the time. Additionally, stronger isolated cells were more likely to contain an HZC—cells whose reflectivity exceeded 40 dBZ at some point developed an HZC 10% of the time, and cells with a maximum reflectivity over 50 dBZ had an HZC 34% of the time.

Figure 7 shows statistics on the duration, formation time, area, and height of HZCs. The vast majority of HZCs (>80%) were short-lived, lasting less than 10 min (Fig. 7a). In reality there is likely additional variability within the 0–10-min bin in this histogram; however, because horizontal scans were only taken every 10 (15) min in 2019 (2018), 10 min is the finest interval that can be resolved. These short-lived HZCs were approximately equally likely to be found in both long- and short-lived parent cells. Figure 7b shows the formation time of HZCs, defined as the time between the formation of a given isolated cell, and the time at which an HZC was first observed. The majority (65%) of HZCs appeared in 20 min or less after cell initiation, or within 1–2 SEA-POL scans. In isolated

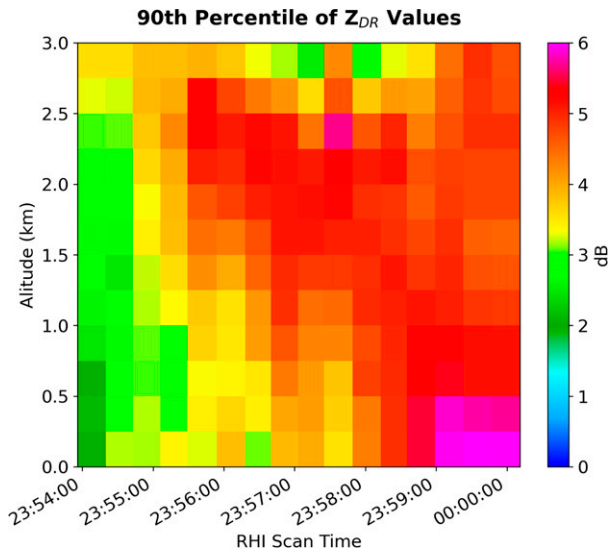


FIG. 6. Vertical profiles of the 90th percentile of Z_{DR} values from the scans depicted in Fig. 5. The color at each grid box corresponds to the 90th percentile of Z_{DR} values at a given altitude (y axis) during a given scan (x axis).

cells which had at least one HZC, the HZC lasted 11% of the cell's entire lifetime on average.

The majority of HZCs were quite small, with a mean area of 8 km^2 . By definition (described in the preceding paragraph), 5 km^2 is the smallest possible HZC size (owing to the interpolation grid size), so it is the smallest bin size used here. Figure 7d shows both the height of HZCs (blue bars) as well as the height of minimum detectable reflectivity echo tops above the HZCs (orange bars). The majority of HZCs were shallow, with a mean height of 3.7 km, with 87% of the HZCs topping out at or below the freezing level (5 km). The reflectivity above the HZCs was also typically shallow, and on average extended 1.6 km above the HZC. However, it should be noted that approximately half of isolated cells with HZCs had reflectivity echo tops that extended above the freezing level. This brings us to an important distinction. While a warm rain cell is technically defined as a cell which is confined entirely below the freezing level (Glickman 2000), this is different from a cell which exhibits warm rain processes. That is to say, even in a cell which has some cloud mass in a subfreezing environment, and therefore could contain ice, there may still be substantial collision–coalescence drop growth (Johnson et al. 1999; Lau and Wu 2003). Johnson et al. (1999) argued that cumulus congestus clouds (defined as radar echoes with tops between 4.5 and 9.5 km) may not fully glaciate until reaching temperatures of around -15°C , and that significant amounts of supercooled liquid water can exist in these clouds at temperatures between -10° and -15°C . When the cells are short lived, as is the case for many small isolated cells, this likely reduces the probability of freezing even further. For these reasons, HZCs within isolated cells that extend above the freezing altitude will be treated the same as those in pure warm rain clouds for the purposes of this paper. While we acknowledge

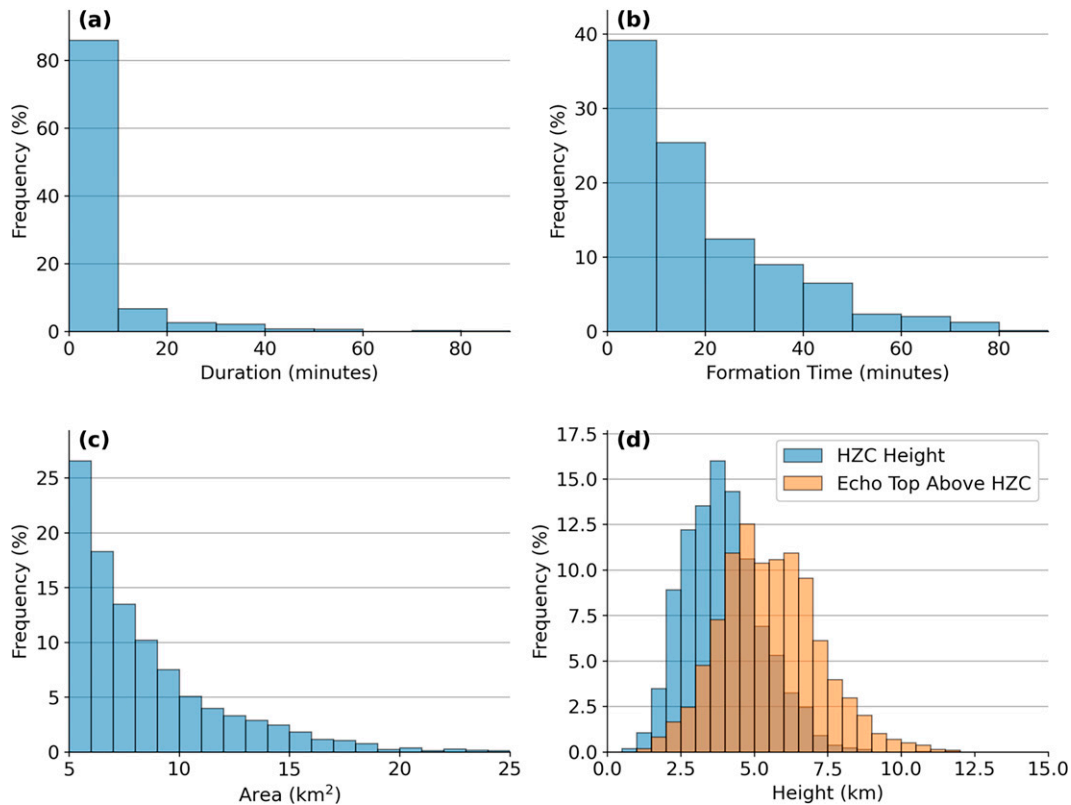
High- Z_{DR} Core Statistics

FIG. 7. (a) Duration, (b) formation time, (c) area, and (d) height of high Z_{DR} cores (HZCs). The height of the HZC (blue bars) as well as the maximum height of reflectivity above the HZC (orange) are also shown in (d).

that some ice and freezing/melting may exist in these storms, we argue that warm rain processes are the predominant mechanism for rain production in most cases.

b. HZC cell structure

Figure 8 shows the location of HZC pixels in isolated cells relative to the wind direction. High Z_{DR} pixels were primarily found on the upwind side of cells, with 75% of high Z_{DR} pixels located upwind of the echo center. We hypothesize that this pattern is caused by size sorting, wherein the horizontal advection of smaller drops is more substantial than large drops. As drops begin to grow and the drop size distribution within the cell broadens, the smaller drops are transported downwind, leaving mainly large drops on the upwind side. This would result in enhanced Z_{DR} on the upwind side. Although high Z_{DR} frequency appears to decrease on the downwind side of these cells, this does not necessarily mean that the large drops are entirely absent there. Despite the fact that reflectivity is proportional to the sixth power of drop diameter, and therefore Z_{DR} will be strongly influenced by the largest oblate drops, in the case where a high number concentration of small drops is mixed with a very low concentration of large drops, the Z_{DR} signal can be dominated by the quasi-spherical smaller drops, producing a smaller Z_{DR} (as well as an increase in K_{DP} , as will be discussed later).

Hence, it is possible that the large drops may still exist in regions of more modest Z_{DR} . High Z_{DR} values may only arise when/if the size sorting mechanism discussed above isolates the large drops by themselves on the upwind side, and masks the high Z_{DR} signal on the downwind side by locally increasing the concentration of small drops. This effect of small drops masking the high Z_{DR} signal of large drops is investigated further in section 4c).

Looking now at vertical structure, Fig. 8 shows that HZC pixels were more frequently found in the lower levels of echoes, with a maximum around 1 km. Below 1 km the frequency drops off, although this is likely due to under sampling as a result of the radar-beam overshooting the near-surface levels at far ranges. The increase in high Z_{DR} frequency with lower altitudes may be due to a few reasons. As the drops fall from cloud top, they likely continue to grow through collision-coalescence and increase in size, which would lead to a higher Z_{DR} . Additionally, the temperature of the raindrops may also play a significant role given the sensitivity of the dielectric constant to temperature. At higher temperatures, the spike in Z_{DR} in the Mie scattering region Fig. 2 is larger, so the increase in high Z_{DR} pixel frequency at low levels may also be attributed to the warmer air nearer to the ocean surface (Zrnić et al. 2000). This temperature effect is discussed further in section 4c). Finally, continued size-sorting

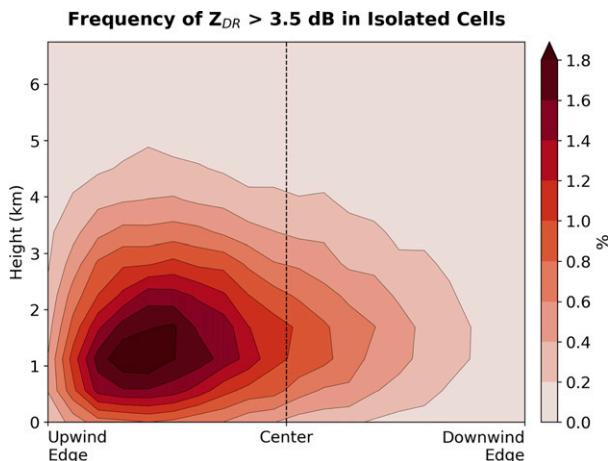


FIG. 8. Heatmap of the location pixels with high Z_{DR} within HZC cells. The center is calculated as the center-of-mass of all pixels (not weighted by reflectivity) within the cell, and edges are defined as the furthest upwind/downwind point from center.

as drops fall may lead to a further enhancement of Z_{DR} closer to the surface, as seen in Kumjian and Ryzhkov (2012).

Figure 9 shows the structure of radar variables within HZC cells. The overall picture is consistent with the idea of a cell with drops which have been sorted such that primarily large drops remain on the upwind side. Note that while the maximum in Z_{DR} occurs at the far upwind edge, the maximum in specific differential phase (K_{DP}) is displaced further downwind. Because K_{DP} is proportional to total liquid

water content and mass weighted oblateness (Bringi and Chandrasekar 2001), the fact that the Z_{DR} maximum lies in a region of lower K_{DP} suggests that the far upwind edge of these HZC cells is composed of very large drops, but at low concentrations, constituting small liquid water contents. This separation of K_{DP} and Z_{DR} maxima has been shown to be indicative of size sorting (e.g., Kumjian and Ryzhkov 2012; Loeffler and Kumjian 2020; Homeyer et al. 2020), further supporting the idea that separation of large and small drops is occurring in these cells. Correlation coefficient (ρ_{hv}), a measurement of the homogeneity (or lack thereof) of scatterers within a beam volume, is also at a minimum at the far upwind edge. These depressed values of ρ_{hv} are likely due to increased values of backscatter differential phase caused by raindrops with diameters well into the Mie scattering region. In these situations, ρ_{hv} can be as low as 0.93 at C band (Balakrishnan and Zrnić 1990; Ryzhkov and Zrnić 2019). The location of the Z_{DR} maximum on the upwind edge, slightly offset from the K_{DP} maximum, also suggests the presence of an updraft on the upwind side, where large drops are expected to be sourced.

Vertically, the upwind edge shows an increase in Z_{DR} as altitude decreases. This again demonstrates the possible impact of drop growth as well as increasing temperature (Zrnić et al. 2000) and continued size sorting (Kumjian and Ryzhkov 2012) on Z_{DR} . As drops fall, they warm and continue to grow, both of which enhance Z_{DR} . Sedimentation size sorting, wherein large drops fall out quicker compared to smaller ones (Kumjian and Ryzhkov 2012) may also be playing a role.

Further downwind, significant concentrations of smaller drop sizes begin to mix in, leading to maxima in reflectivity

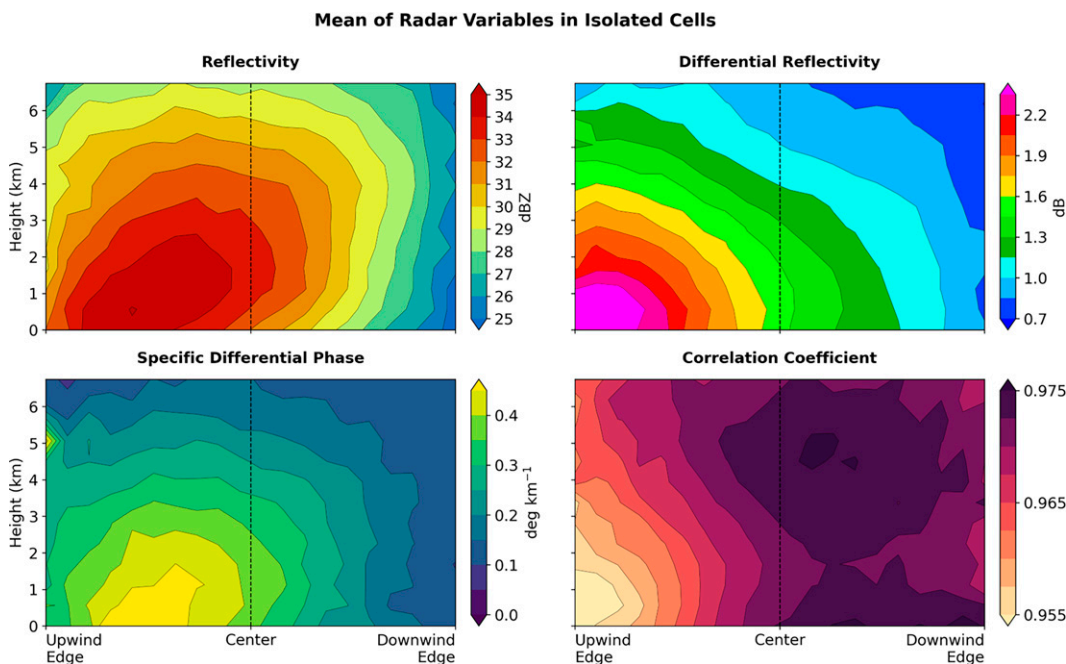


FIG. 9. As in Fig. 8, but looking at the mean values of (a) reflectivity, (b) differential reflectivity, (c) specific differential phase, and (d) correlation coefficient.

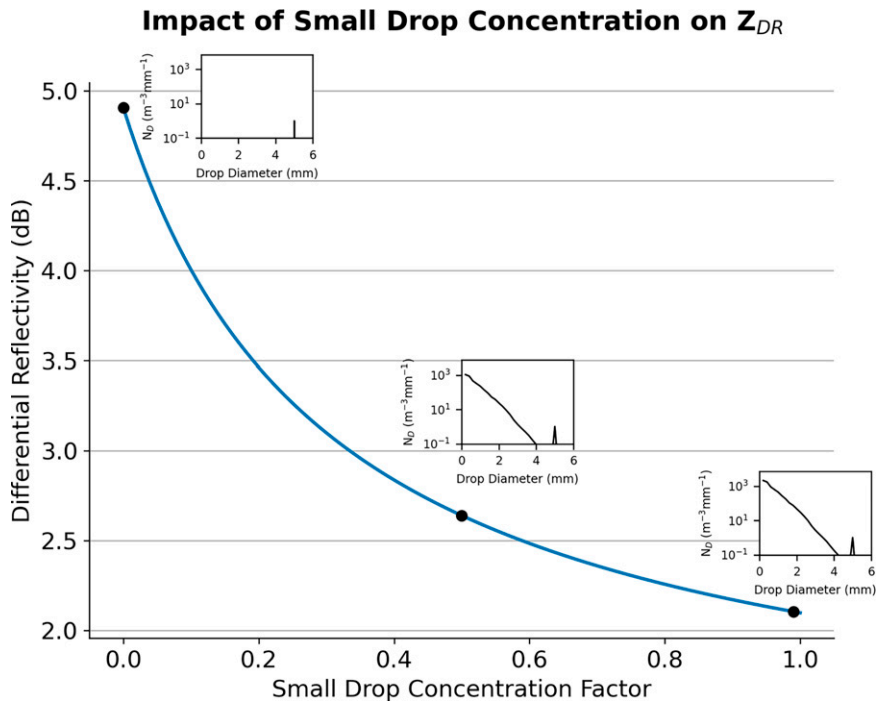


FIG. 10. Calculated Z_{DR} vs concentration of small drops. Baseline small drop concentration factor was determined by averaging disdrometer data from cells with light-to-moderate rain, and then multiplied by a “concentration factor” on the x axis and combined with a set concentration of large (5 mm) drops. Inset plots show the drop distribution at selected points along the line. Calculations were performed for a radar with a SEA-POL frequency (5.65 GHz), with all of the same scattering parameters outlined in the caption of Fig. 2.

and K_{DP} , while Z_{DR} begins to decrease either due to the masking effect discussed previously, or due to absence of large drops. Moving past the center to the downwind side, reflectivity, K_{DP} , and Z_{DR} , all decrease as ρ_{hv} increases. This suggests that the downwind side of HZC cells are composed primarily of light rain or drizzle with near uniform quasi-spherical drops, potentially blown in from the upwind side.

c. Scattering simulations

We now explore the theoretical basis for some of the observations of HZCs described above. This section will investigate simulated Z_{DR} for given drop size distributions. As discussed above, it is hypothesized that large drops may exist outside of high Z_{DR} regions due to the masking effect of small drops. This is demonstrated in Fig. 10, which shows the simulated Z_{DR} of large drops mixed with varying concentrations of small drops. When no small drops are included in the scattering calculations (left side of Fig. 10), the simulated Z_{DR} is nearly 5 dB, similar to what was observed by SEA-POL on the upwind side of the HZC cells. However, as small drops are mixed in, Z_{DR} rapidly decreases. When the full small drop concentration is applied, Z_{DR} drops to ~ 2 dB. It is noted here that this method of mixing a typical small-drop concentration with a monodisperse large drop concentration does not necessarily result in a drop concentration representative of what one would realistically observe within an HZC cell. However,

the intent of this method is not to create realistic drop size distributions, but to test the sensitivity of Z_{DR} to mixture of large and small drops in general. Toward that end, these results suggest that even when the Z_{DR} in tropical convection is measured at more typical levels (1–2 dB), this does not preclude the existence of large drops in that same radar volume. This relationship between Z_{DR} and median drop diameter as a function of maximum drop size is investigated further in Carey and Petersen (2015).

It was also noted previously that the frequency of high Z_{DR} pixels was higher at lower altitudes, where temperatures are generally higher. Based on sounding data, the ambient atmospheric temperature increased over 20°C from 7.7°C at 3.7 km (the mean height of HZCs) to 28°C at the surface. Figure 11 shows the sensitivity of Z_{DR} scattering calculations to water drop temperature due to the dielectric effect. In the Mie scattering regime, temperature has a significant impact on Z_{DR} . For example, a 5.5-mm drop at near-freezing temperatures would have a Z_{DR} of 5.5 dB, while a drop at 25°C (the approximate surface mean wet-bulb temperature during PISTON) would have a Z_{DR} of 8.3 dB. While these calculations are for a monodisperse distribution, and the impact of temperature would likely be less for a more realistic drop size distribution, the overall impact of temperature remains the same. As drops fall and warm, their Z_{DR} may increase even if their size remains constant (i.e., Zrníć et al. 2000). This effect could

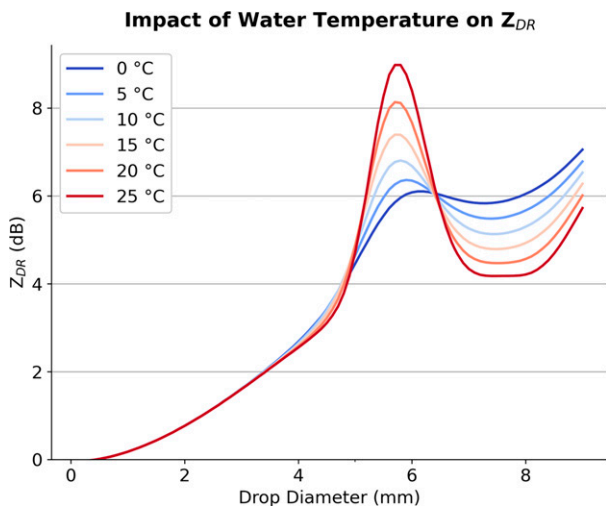


FIG. 11. As in Fig. 2, but calculated for different water temperatures.

partially explain the increase in the frequency of high Z_{DR} pixels at lower altitudes.

d. Drop growth

This section will investigate the growth of drops in tropical warm rain under different microphysical regimes. Figure 12 shows the growth trajectory of a water drop under varying background LWCs. In all LWC scenarios, large drops (>4.5 mm) formed by the time the drop exited cloud base. Interestingly, the final drop diameter for all LWC scenarios is approximately equal. Although drops do grow more slowly in low LWC conditions, slower growth allows them to be lofted higher in the cloud. Therefore, the slow growth rate at low LWCs is offset by a longer cloud residence time, and the final drop size is similar. However, at a LWC of 1 g m^{-3} , it takes nearly a full hour for the drop to exit the cloud. The majority of HZC cells observed during PISTON formed in 20 min or less (Fig. 7), so this suggests that high cloud LWCs ($>2 \text{ g m}^{-3}$) must have been commonly present during PISTON operations. While Szumowski et al. (1998) generally found that LWC values were less than 1.5 g m^{-3} during HaRP, they suggest that this may be an underestimate due to instrument limitations. Additionally, aircraft observations of HZC cells during PISTON (discussed in section 3a) observed LWCs $> 2 \text{ g m}^{-3}$, so this is a reasonable value to expect. Drop sizes at the highest point of these trajectories are all around 0.8 mm, which is close to the 1-mm drops at cloud top observed by Szumowski et al. (1998).

Figure 13 shows similar drop growth trajectories, but calculated for different updraft speeds while holding LWC constant at 1.5 g m^{-3} . Generally, as updraft speed increases, the final drop size upon exiting cloud base increases. While a 1 m s^{-1} updraft is too weak to support large drop formation (final drop size is less than 1 mm in this scenario), stronger updrafts of 3 and 5 m s^{-1} were found to produce drops of 4.2 and 10 mm, respectively. The latter is probably unrealistically large, and arises due to the limitations of this simple model (e.g., breakup is not considered). In reality, a 5 m s^{-1}

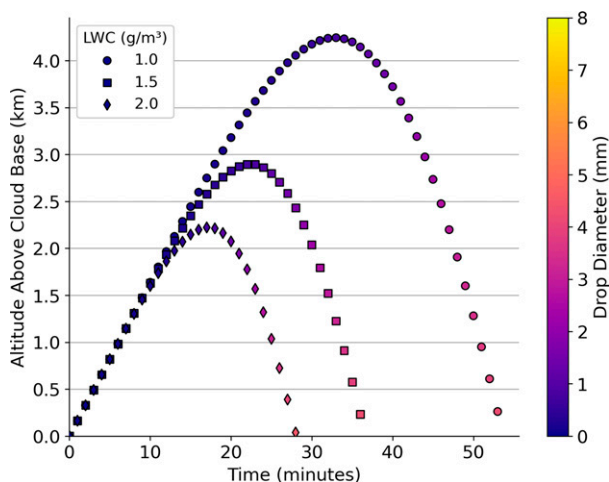


FIG. 12. Time series of drop growth using the continuous collection equation under different background liquid water contents (LWC). A constant updraft speed of 3 m s^{-1} was used in these calculations.

updraft would be unlikely to last for 50+ min as is shown in this plot, and the drop would probably not remain within the updraft core for that entire time even if it did. During PISTON, HZC cells had echo tops as low as 3 km. This is approximately the maximum elevation reached by the drop in the 3 m s^{-1} updraft scenario. Evidently, with this simple model, a LWC of 1.5 g m^{-3} and an updraft speed of 3 m s^{-1} is sufficient to explain the formation of 4.5-mm drops in very shallow convection.

We note here that while in this simple drop growth model drops only obtained a diameter of ~ 0.8 mm at cloud top (theoretically not large enough to induce Mie scattering), these are much smaller than the drops at cloud top in the RHIs presented in section 3b), which were evidently large enough to induce Mie scattering and high Z_{DR} values. Rapid drop growth at cloud top may be a result of rapid collection of small drops suspended above the updraft (Szumowski et al. 1997, 1999), or even a recirculation of drops (e.g., Rauber et al. 1991), both of which are not accounted for in the simple collection model. Furthermore, the rate at which large drops formed in the RHIs is much faster than what was predicted by the continuous collection model. One potential explanation for this is that while in the model drops were initialized at the size of a condensing sea salt aerosol ($20 \mu\text{m}$), the radar scans used in the case study (section 3b) begin after substantial drop growth had already occurred. Under the continuous collection model, drop growth rate increases with time—in the 1.5 g m^{-3} LWC, 3 m s^{-1} updraft scenario, the drop diameter increases to 1 mm in the first 25 min, and then to 4.2 mm in the next 10 min. This latter, rapid drop growth stage is what is observed in the RHI case study (although we note that the magnitude of the growth rate in the case study is still more rapid than even the latter stages of the model). Were the full life cycle of the storm observed (including early growth prior to precipitation onset), it is expected that the time to detect

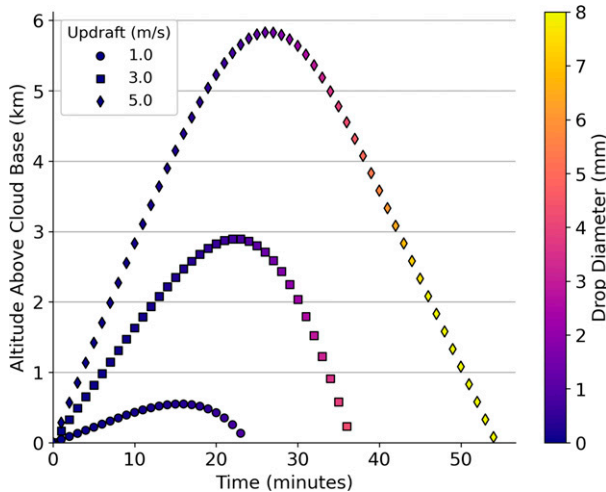


FIG. 13. As in Fig. 12, but with varying updraft speeds and liquid water content held constant at 1.5 g m^{-3} .

large Z_{DR} values would be closer to what is predicted by the continuous collection model. Furthermore, the simple collection model is known to underestimate drop growth (Berry and Reinhardt 1974; Yau and Rogers 1996), so the times predicted by this model are likely overestimates of how long it would take to form large drops.

e. HZC cell location

To this point, only HZCs observed within small, isolated convective cells have been considered. However, HZCs did occasionally occur in the convective portions of larger, more organized precipitation features, which we refer to as non-isolated convection. The following section will address this.

Figure 14 shows the distribution of Z_{DR} values within isolated and non-isolated convective features. To emphasize the differences in the tail of the histogram, which makes up a relatively small fraction of the overall distribution but is the primary interest of this study (large Z_{DR}), a log-y axis is used in this plot. Large Z_{DR} values are much more common in isolated cells compared to non-isolated cells. Based on our observations in PISTON convective elements within non-isolated features were typically deeper and longer lived, implying that ice and freezing/melting processes may be present in these features (non-isolated features had a mean echo top height of 8.1 km and an average lifetime of about 100 min, compared to 4.5 km and 15 min for isolated features). Recall that for large drops to form, it is hypothesized that a “clean” updraft channel is required (Raubert et al. 1991; Szumowski et al. 1999), free of any small drops which would cause collisional break-up of the large drops, or compete for available cloud water with drops formed within the updraft, thereby limiting their size. One such source of the small drops would be due to the melting of ice falling from the subfreezing portion of the convection. Another mechanism to explain the lower Z_{DR} values in non-isolated convection (Fig. 14) is that smaller drops are present (from the melting of ice) which would work to mask the high Z_{DR} signature of the large drops (as discussed in section 4c).

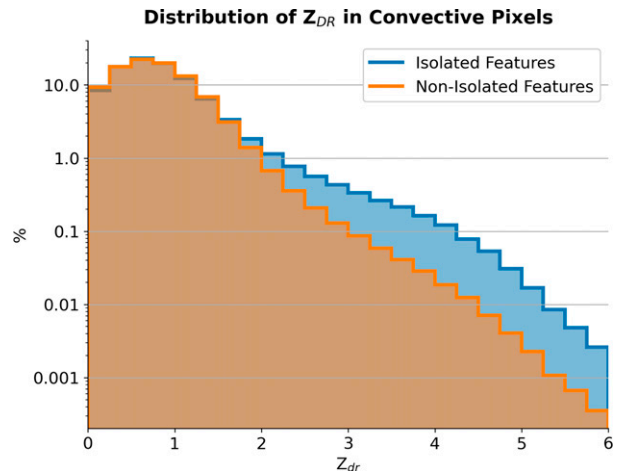


FIG. 14. Distribution of differential reflectivity (Z_{DR}) within convective pixels for isolated (blue) and non-isolated (orange) pixels, as classified by the Steiner et al. (1995) algorithm. Distribution has been plotted on a log-y axis to emphasize the differences at the extreme right tail.

However, as was mentioned previously, large, organized features did occasionally contain HZCs, despite extensive amounts of ice and melting existing within the feature. One clue as to how this may happen lies within the location of HZCs within these features. Although it is not directly quantified in the present study, in general it was noted that HZCs within MCS during PISTON typically occurred on the leading convective edges. An example of this is provided in Fig. 15. The convective line on the leading edge of this southward-propagating MCS is dotted with numerous individual HZCs. Although high reflectivity values exist elsewhere in the storm, only the extreme southern edge of the leading line has any high Z_{DR} signal. Analysis of vertical RHI cross sections through this leading edge (not shown) reveal that this convection topped out below the freezing level, and a hydrometeor identification algorithm detected no graupel/hail, suggesting that the high Z_{DR} signal is arising from large drops, rather than rimed particles. The convection here is young, relatively shallow, and removed from the extensive region of stratiform (and associated ice processes) behind it. Strong updrafts along the leading edge (likely associated with cold pool propagation) are evidently enough to initiate the formation of large drops.

5. Conclusions

In this study, we discussed isolated convection observed by the SEA-POL radar during the PISTON field campaign, marked by very large Z_{DR} values, denoting the presence of large ($>4.5 \text{ mm}$) raindrops. While such drop sizes are commonly observed in the midlatitudes and often form from melting ice, the majority of the convective cells examined in this study had echo tops which were near or below the freezing altitude, implying that these large drops were produced through warm rain processes (i.e., collision-coalescence). While large

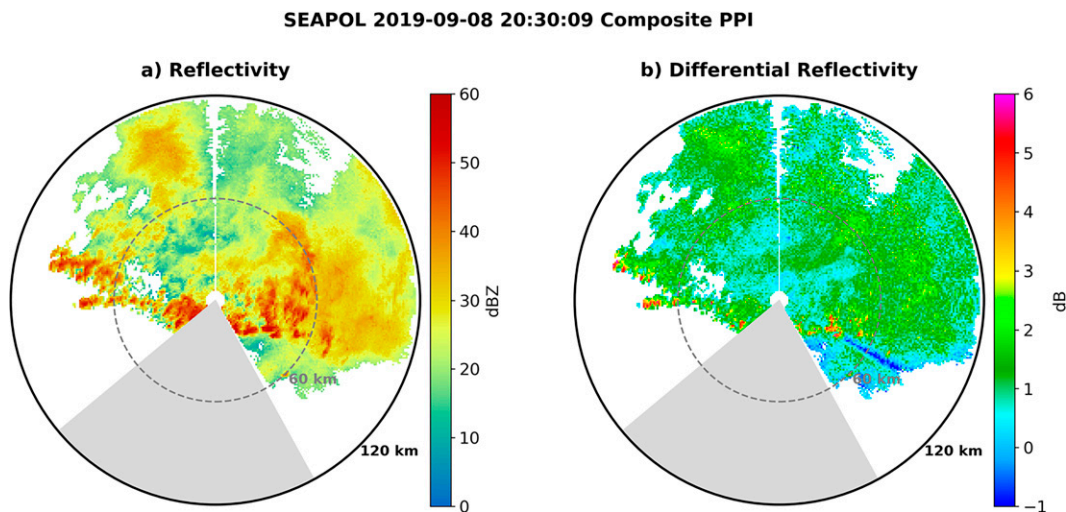


FIG. 15. Example of a large convective system with areas of high Z_{DR} on the leading convective edge on the south side.

drops in tropical warm rain have been observed and studied previously (Beard et al. 1986; Rauber et al. 1991; Takahashi et al. 1995; Szumowski et al. 1997, 1998, 1999; Hobbs and Rangno 2004), these studies focused primarily on individual case studies. And while Gatlin et al. (2015) did provide a statistical overview of the occurrence of large drops, they did not have the ability to distinguish whether these drops formed from warm- or cold-rain processes. The current study takes advantage of the extensive PISTON dataset and leverages the polarimetric capabilities of SEA-POL to study these large drop producing cells in a more statistical manner, looking at the average structure and characteristics of the HZCs themselves as well as the cells they occur in. Cells were also examined on a case-study level in this research, utilizing rapid vertical cross-section scans performed by SEA-POL, as well as in situ drop size distribution measurements made by aircraft which transected the storms.

The majority of HZC cells were small (mean area of 8 km^2), formed quickly (within 20 min of the first detection by SEA-POL of the parent cell), and were short-lived (usually <10 min). Although the high Z_{DR} regions themselves predominately existed below the 5 km freezing altitude (mean height of 3.7 km, 87% below 5 km), approximately half of HZCs existed within a cell which had echo tops above the freezing level. In deeper cumulus congestus clouds like these, particularly in the tropics where warm cloud depths are large and cloud water content is high, glaciation may be slow to occur (Johnson et al. 1999; Lau and Wu 2003). Therefore, we argue that although some ice/cold-rain processes may be ongoing in these taller cells, they are still predominately warm-rain based, and the high Z_{DR} /large raindrops are due primarily to collision-coalescence. Similarly, HZCs were occasionally found within large MCSs, which certainly have extensive regions of stratiform and cold-rain processes. However, it was found that HZCs within these MCSs were typically located on the outer edges of the leading convective lines, likely triggered by

cold pool propagation. The young convection on the edges of these complexes were well removed from the stratiform regions within the MCSs, and thus the large drops are again expected to have developed through primarily warm rain processes.

The average structure of isolated cells with HZCs were examined by looking at composite polarimetric radar variables in an upwind/downwind-height parameter space. A distinct size-sorting signal was evident, with the highest Z_{DR} values located on the upwind-edge of cells, along with low K_{DP} , suggesting this region is composed of a small concentration of large drops. Closer to the center, Z_{DR} began to decrease as reflectivity and K_{DP} increase, suggesting a mixture of large and small drops. Although the high Z_{DR} signal dissipates near cell-center, scattering simulations indicate that this may be due to a masking of the signal by a high concentration of smaller drops, rather than the large drops themselves vanishing. On the downwind half of HZC cells, Z_{DR} , reflectivity, and K_{DP} all decrease as correlation coefficient increases, suggesting this region is composed of numerous, uniform, spherical small drops (light rain or drizzle), also a result of wind-driven size-sorting. Vertically, Z_{DR} tended to be higher at lower levels of these cells. This is likely due to a combination of continuing growth of drops through coalescence (Figs. 8, 9), and higher temperatures at lower altitudes, leading to increased Mie resonance effects caused by an increasing dielectric constant (Fig. 11), and continued size-sorting of drops as the fall to lower levels (Kumjian and Ryzhkov 2012). These findings were supported by theoretical models, in situ aircraft measurements of drop size distributions in an HZC, as well as a case study which utilized rapid vertical cross-section scans of a shallow cell with an HZC.

Using a simple collection model, drop growth was simulated under various LWC and updraft scenarios. With this model, it was found that although all LWCs could theoretically support the formation of large drops provided a moderate 3 m s^{-1} updraft, only the 2 g m^{-3} scenario produced

large drops at the time scales observed during PISTON (<20 min). While sampling an HZC cell, the Learjet recorded LWCs in excess of 2 g m^{-3} , so this value is not unreasonable. Still, HZCs which took 60 or more minutes to form were occasionally observed, so extreme LWCs may be a sufficient but not necessary condition for large drop formation, given updrafts are sustained for long enough.

One outstanding question not addressed by this study is the impact of the environment on the abundance of large drop-producing warm rain cells. While it is tempting to try to correlate environmental conditions (i.e., sea salt aerosol concentration, instability, moisture levels, vertical wind shear) to HZC abundance as seen by SEA-POL, this would unfortunately not suffice to answer the proposed question. The primary limiting factor here is that, due to the masking effect discussed previously, one cannot equate a lack of an HZC signal to the absence of large drops. That is, cells which have large drops embedded within them may not have a high Z_{DR} signature if these drops are mixed in with numerous smaller drops. Therefore, a time series of some metric that measures *HZC presence* may not be the same as a time series that depicts the presence of *large drops*. Therefore, a statistical correlation (or lack thereof) drawn between environmental variables and HZCs does not necessarily represent the relation between those environmental variables and large drops. Unfortunately, with the data collected during PISTON, we are unable to attain a time series of the actual drop size distribution within each cell observed, so the question of the environmental influence on large drop formation is beyond the scope of this study.

While tracking HZC cells became a focus of the campaign as it was underway, PISTON was not specifically designed as a project for this topic, and thus there were factors limiting how optimally HZC data could be collected. Isolated cells are small and short lived, and were difficult to capture full life cycles. Scanning strategies could be developed which are more optimal for capturing the evolution of individual cells at a high spatial and temporal resolution. Additionally, the use of an S-band radar would mitigate Mie scattering effects encountered by the SEA-POL C-Band radar, and allow for full DSD retrievals to be more easily obtained from polarimetric data. While polarimetric radar data can provide some information on the microphysical aspects of storms, the true drop size distribution (and presence/concentration of large drops) cannot be known without in situ measurements from disdrometer and particle probes, particularly measurements from instruments on aircraft which can make multiple, targeted transects through storms, and maneuver quickly enough to intersect these small cells. While aircraft data were used in JHWRP and HaRP to learn about large drops in warm rain, the radar observations in these projects were not dual-polarized. The additional microphysical insights provided by polarimetric radars such as SEA-POL provide exciting new context to place the aircraft observations in. While one HZC was observed simultaneously by SEA-POL and the CAMP²Ex Learjet, these observations were again suboptimal due to it not being the primary focus of either campaign. A future project which was designed specifically to address many of the topics and questions brought up in this study would be

very beneficial in learning about these storms, and may lead to advances in how they are parameterized in models, which itself could have broad implications.

Acknowledgments. This research was funded by the Office of Naval Research Grant N00014-16-1-3092. Thanks to Paul Lawson at SPEC Inc. for generously providing the particle probe data from the Learjet used in this study. Special thanks to the crews of the PISTON ships, the *R/V Thomas G. Thompson* and *R/V Sally Ride*, for allowing and assisting with the set-up of SEA-POL on these ships.

Data availability statement. Data collected by SEA-POL radar and CAMP²Ex aircraft are available at <https://www-air.larc.nasa.gov/cgi-bin/ArcView/camp2ex>. KuPR swaths are available at https://disc.gsfc.nasa.gov/datasets/GPM_2AKu_06/summary (DOI:10.5067/GPM/DPR/Ku/2A/06).

REFERENCES

- Balakrishnan, N., and D. S. Zrnić, 1990: Use of polarization to characterize precipitation and discriminate large hail. *J. Atmos. Sci.*, **47**, 1525–1540, [https://doi.org/10.1175/1520-0469\(1990\)047<1525:UOPTCP>2.0.CO;2](https://doi.org/10.1175/1520-0469(1990)047<1525:UOPTCP>2.0.CO;2).
- Beard, K. V., and C. Chuang, 1987: A new model for the equilibrium shape of raindrops. *J. Atmos. Sci.*, **44**, 1509–1524, [https://doi.org/10.1175/1520-0469\(1987\)044<1509:ANMFTE>2.0.CO;2](https://doi.org/10.1175/1520-0469(1987)044<1509:ANMFTE>2.0.CO;2).
- , D. B. Johnson, and D. Baumgardner, 1986: Aircraft observations of large raindrops in warm, shallow, convective clouds. *Geophys. Res. Lett.*, **13**, 991–994, <https://doi.org/10.1029/GL013i010p00991>.
- Berry, E. X., and R. L. Reinhardt, 1974: An analysis of cloud drop growth by collection: Part I. Double distributions. *J. Atmos. Sci.*, **31**, 1814–1824, [https://doi.org/10.1175/1520-0469\(1974\)031<1814:AAOCDG>2.0.CO;2](https://doi.org/10.1175/1520-0469(1974)031<1814:AAOCDG>2.0.CO;2).
- Brandes, E. A., G. Zhang, and J. Vivekanandan, 2004: Drop size distribution retrieval with polarimetric radar: Model and application. *J. Appl. Meteor. Climatol.*, **43**, 461–475, [https://doi.org/10.1175/1520-0450\(2004\)043<0461:DSDRWP>2.0.CO;2](https://doi.org/10.1175/1520-0450(2004)043<0461:DSDRWP>2.0.CO;2).
- Bringi, V. N., and V. Chandrasekar, 2001: *Polarimetric Doppler Weather Radar: Principles and Applications*. Cambridge University Press, 636 pp.
- , —, P. Meischner, J. Hubbert, and Y. Golestani, 1991: Polarimetric radar signatures of precipitation at S and C-bands. *IEE Proc. F. Radar Signal Process.*, **138**, 109–119, <https://doi.org/10.1049/ip-f-2.1991.0017>.
- , —, J. Hubbert, E. Gorgucci, W. L. Randeu, and M. Schoenhuber, 2003: Raindrop size distribution in different climatic regimes from disdrometer and dual-polarized radar analysis. *J. Atmos. Sci.*, **60**, 354–365, [https://doi.org/10.1175/1520-0469\(2003\)060<0354:RSDIDC>2.0.CO;2](https://doi.org/10.1175/1520-0469(2003)060<0354:RSDIDC>2.0.CO;2).
- , C. R. Williams, M. Thurai, and P. T. May, 2009: Using dual-polarized radar and dual-frequency profiler for DSD characterization: A case study from Darwin, Australia. *J. Atmos. Oceanic Technol.*, **26**, 2107–2122, <https://doi.org/10.1175/2009JTECHA1258.1>.
- Carey, L. D., and W. A. Petersen, 2015: Sensitivity of C-Band polarimetric radar-based drop size estimates to maximum diameter. *J. Appl. Meteor. Climatol.*, **54**, 1352–1371, <https://doi.org/10.1175/JAMC-D-14-0079.1>.

- Chudler, K., and S. A. Rutledge, 2021: The coupling between convective variability and large-scale flow patterns observed during PISTON 2018–19. *J. Climate*, **34**, 7199–7218, <https://doi.org/10.1175/JCLI-D-20-0785.1>
- Ciesielski, P. E., and Coauthors, 2014: Quality-controlled upper-air sounding dataset for DYNAMO/CINDY/AMIE: Development and corrections. *J. Atmos. Oceanic Technol.*, **31**, 741–764, <https://doi.org/10.1175/JTECH-D-13-00165.1>
- Dawson, D. T., E. R. Mansell, and M. R. Kumjian, 2015: Does wind shear cause hydrometeor size sorting? *J. Atmos. Sci.*, **72**, 340–348, <https://doi.org/10.1175/JAS-D-14-0084.1>
- Dixon, M., and G. Wiener, 1993: TITAN: Thunderstorm Identification, Tracking, Analysis, and Nowcasting—A radar-based methodology. *J. Atmos. Oceanic Technol.*, **10**, 785–797, [https://doi.org/10.1175/1520-0426\(1993\)010<0785:TTITAA>2.0.CO;2](https://doi.org/10.1175/1520-0426(1993)010<0785:TTITAA>2.0.CO;2)
- Dolan, B., B. Fuchs, S. A. Rutledge, E. A. Barnes, and E. J. Thompson, 2018: Primary modes of global drop size distributions. *J. Atmos. Sci.*, **75**, 1453–1476, <https://doi.org/10.1175/JAS-D-17-0242.1>
- Fridlind, A. M., and Coauthors, 2019: Use of polarimetric radar measurements to constrain simulated convective cell evolution: A pilot study with Lagrangian tracking. *Atmos. Meas. Tech.*, **12**, 2979–3000, <https://doi.org/10.5194/amt-12-2979-2019>
- Gatlin, P. N., M. Thurai, V. N. Bringi, W. Petersen, D. Wolff, A. Tokay, L. Carey, and M. Wingo, 2015: Searching for large raindrops: A global summary of two-dimensional video disdrometer observations. *J. Appl. Meteor. Climatol.*, **54**, 1069–1089, <https://doi.org/10.1175/JAMC-D-14-0089.1>
- Glickman, T., Ed., 2000: *Glossary of Meteorology*. 2nd ed. Amer. Meteor. Soc., 855 pp., <http://glossary.ametsoc.org/>
- Gunn, R., and G. D. Kinzer, 1949: The terminal velocity of fall for water droplets in stagnant air. *J. Atmos. Sci.*, **6**, 243–248, [https://doi.org/10.1175/1520-0469\(1949\)006<0243:TTVOFF>2.0.CO;2](https://doi.org/10.1175/1520-0469(1949)006<0243:TTVOFF>2.0.CO;2)
- Hartmann, D. L., and D. A. Short, 1980: On the use of Earth radiation budget statistics for studies of clouds and climate. *J. Atmos. Sci.*, **37**, 1233–1250, [https://doi.org/10.1175/1520-0469\(1980\)037<1233:OTUOER>2.0.CO;2](https://doi.org/10.1175/1520-0469(1980)037<1233:OTUOER>2.0.CO;2)
- Hobbs, P. V., and A. L. Rangno, 2004: Super-large raindrops. *Geophys. Res. Lett.*, **31**, L13102, <https://doi.org/10.1029/2004GL020167>
- Homeyer, C. R., T. N. Sandmæl, C. K. Potvin, and A. M. Murphy, 2020: Distinguishing characteristics of tornadic and nontornadic supercell storms from composite mean analyses of radar observations. *Mon. Wea. Rev.*, **148**, 5015–5040, <https://doi.org/10.1175/MWR-D-20-0136.1>
- Johnson, R. H., T. M. Rickenbach, S. A. Rutledge, P. E. Ciesielski, and W. H. Schubert, 1999: Trimodal characteristics of tropical convection. *J. Climate*, **12**, 2397–2418, [https://doi.org/10.1175/1520-0442\(1999\)012<2397:TCOTC>2.0.CO;2](https://doi.org/10.1175/1520-0442(1999)012<2397:TCOTC>2.0.CO;2)
- Kumjian, M. R., and A. V. Ryzhkov, 2012: The impact of size sorting on the polarimetric radar variables. *J. Atmos. Sci.*, **69**, 2042–2060, <https://doi.org/10.1175/JAS-D-11-0125.1>
- Lau, K., and H. T. Wu, 2003: Warm rain processes over tropical oceans and climate implications. *Geophys. Res. Lett.*, **30**, 2290, <https://doi.org/10.1029/2003GL018567>
- Lawson, R. P., S. Woods, and H. Morrison, 2015: The microphysics of ice and precipitation development in tropical cumulus clouds. *J. Atmos. Sci.*, **72**, 2429–2445, <https://doi.org/10.1175/JAS-D-14-0274.1>
- Loeffler, S. D., and M. R. Kumjian, 2020: Idealized model simulations to determine impacts of storm-relative winds on differential reflectivity and specific differential phase fields. *J. Geophys. Res. Atmos.*, **125**, e2020JD033870, <https://doi.org/10.1029/2020JD033870>
- Mishchenko, M. I., L. D. Travis, and D. W. Mackowski, 1996: T-matrix computations of light scattering by nonspherical particles: A review. *J. Quant. Spectrosc. Radiat. Transfer*, **55**, 535–575, [https://doi.org/10.1016/0022-4073\(96\)00002-7](https://doi.org/10.1016/0022-4073(96)00002-7)
- Petty, G. W., 1999: Prevalence of precipitation from warm-topped clouds over eastern Asia and the western Pacific. *J. Climate*, **12**, 220–229, [https://doi.org/10.1175/1520-0442\(1999\)012<0220:POPFWT%3E2.0.CO;2](https://doi.org/10.1175/1520-0442(1999)012<0220:POPFWT%3E2.0.CO;2)
- Pruppacher, H. R., and J. D. Klett, 1978: Hydrodynamics of single cloud and precipitation particles. *Microphysics of Clouds and Precipitation*, 1st ed. H. R. Pruppacher and J. D. Klett, Eds., Springer, 282–346, https://doi.org/10.1007/978-94-009-9905-3_10
- Rauber, R. M., K. V. Beard, and B. M. Andrews, 1991: A mechanism for giant raindrop formation in warm, shallow convective clouds. *J. Atmos. Sci.*, **48**, 1791–1797, [https://doi.org/10.1175/1520-0469\(1991\)048<1791:AMFGRF>2.0.CO;2](https://doi.org/10.1175/1520-0469(1991)048<1791:AMFGRF>2.0.CO;2)
- Rickenbach, T. M., and S. A. Rutledge, 1998: Convection in TOGA COARE: Horizontal scale, morphology, and rainfall production. *J. Atmos. Sci.*, **55**, 2715–2729, [https://doi.org/10.1175/1520-0469\(1998\)055<2715:CITCHS>2.0.CO;2](https://doi.org/10.1175/1520-0469(1998)055<2715:CITCHS>2.0.CO;2)
- Rutledge, S. A., V. Chandrasekar, B. Fuchs, J. George, F. Junyent, B. Dolan, P. C. Kennedy, and K. Drushka, 2019a: SEA-POL goes to sea. *Bull. Amer. Meteor. Soc.*, **100**, 2285–2301, <https://doi.org/10.1175/BAMS-D-18-0233.1>
- , —, —, —, —, P. Kennedy, and B. Dolan, 2019b: Deployment of the SEA-POL C-band polarimetric radar to SPURS-2. *Oceanography*, **32**, 50–57, <https://doi.org/10.5670/oceanog.2019.212>
- Ryzhkov, A. V., and D. S. Zmić, 2019: *Radar Polarimetry for Weather Observations*. Springer, 504 pp.
- Schumacher, C., M. H. Zhang, and P. E. Ciesielski, 2007: Heating structures of the TRMM field campaigns. *J. Atmos. Sci.*, **64**, 2593–2610, <https://doi.org/10.1175/JAS3938.1>
- Slingo, A., 1990: Sensitivity of the Earth's radiation budget to changes in low clouds. *Nature*, **343**, 49–51, <https://doi.org/10.1038/343049a0>
- Sobel, A. H., J. Sprintall, E. D. Maloney, Z. K. Martin, S. Wang, S. P. de Szoeke, B. C. Trabling, and S. A. Rutledge, 2021: Large-scale state and evolution of the atmosphere and ocean during PISTON 2018. *J. Climate*, **34**, 5017–5035, <https://doi.org/10.1175/JCLI-D-20-0517.1>
- Steiner, M., R. A. Houze Jr., and S. E. Yuter, 1995: Climatological characterization of three-dimensional storm structure from operational radar and rain gauge data. *J. Appl. Meteor.*, **34**, 1978–2007, [https://doi.org/10.1175/1520-0450\(1995\)034<1978:CCOTDS>2.0.CO;2](https://doi.org/10.1175/1520-0450(1995)034<1978:CCOTDS>2.0.CO;2)
- Stephens, G. L., and Coauthors, 2002: The CloudSat mission and the A-Train: A new dimension of space-based observations of clouds and precipitation. *Bull. Amer. Meteor. Soc.*, **83**, 1771–1790, <https://doi.org/10.1175/BAMS-83-12-1771>
- Szumowski, M. J., R. M. Rauber, H. T. Ochs, and L. J. Miller, 1997: The microphysical structure and evolution of Hawaiian rainband clouds. Part I: Radar observations of rainbands containing high reflectivity cores. *J. Atmos. Sci.*, **54**, 369–385, [https://doi.org/10.1175/1520-0469\(1997\)054<0369:TMSAEO>2.0.CO;2](https://doi.org/10.1175/1520-0469(1997)054<0369:TMSAEO>2.0.CO;2)
- , —, —, and K. V. Beard, 1998: The microphysical structure and evolution of Hawaiian rainband clouds. Part II: Aircraft measurements within rainbands containing high

- reflectivity cores. *J. Atmos. Sci.*, **55**, 208–226, [https://doi.org/10.1175/1520-0469\(1998\)055<0208:TMSAEO>2.0.CO;2](https://doi.org/10.1175/1520-0469(1998)055<0208:TMSAEO>2.0.CO;2).
- , —, and —, 1999: The microphysical structure and evolution of Hawaiian rainband clouds. Part III: A test of the ultraviolet nuclei hypothesis. *J. Atmos. Sci.*, **56**, 1980–2003, [https://doi.org/10.1175/1520-0469\(1999\)056<1980:TMSAEO>2.0.CO;2](https://doi.org/10.1175/1520-0469(1999)056<1980:TMSAEO>2.0.CO;2).
- Takahashi, T., K. Suzuki, M. Orita, M. Tokuno, and R. de la Mar, 1995: Videosonde observations of precipitation processes in equatorial cloud clusters. *J. Meteor. Soc. Japan*, **73**, 509–534, https://doi.org/10.2151/jmsj1965.73.2B_509.
- Thompson, E. J., S. A. Rutledge, B. Dolan, and M. Thurai, 2015: Drop size distributions and radar observations of convective and stratiform rain over the equatorial Indian and west Pacific Oceans. *J. Atmos. Sci.*, **72**, 4091–4125, <https://doi.org/10.1175/JAS-D-14-0206.1>.
- , —, —, —, and V. Chandrasekar, 2018: Dual-polarization radar rainfall estimation over tropical oceans. *J. Appl. Meteor. Climatol.*, **57**, 755–775, <https://doi.org/10.1175/JAMC-D-17-0160.1>.
- Thurai, M., V. N. Bringi, and P. T. May, 2010: CPOL radar-derived drop size distribution statistics of stratiform and convective rain for two regimes in Darwin, Australia. *J. Atmos. Oceanic Technol.*, **27**, 932–942, <https://doi.org/10.1175/2010JTECHA1349.1>.
- Ulbrich, C. W., and D. Atlas, 2007: Microphysics of raindrop size spectra: Tropical continental and maritime storms. *J. Appl. Meteor. Climatol.*, **46**, 1777–1791, <https://doi.org/10.1175/2007JAMC1649.1>.
- Yau, M. K., and R. R. Rogers, 1996: *A Short Course in Cloud Physics*. Elsevier, 304 pp.
- Zrnić, D. S., T. D. Keenan, L. D. Carey, and P. May, 2000: Sensitivity analysis of polarimetric variables at a 5-cm wavelength in rain. *J. Appl. Meteor.*, **39**, 1514–1526, [https://doi.org/10.1175/1520-0450\(2000\)039<1514:SAOPVA>2.0.CO;2](https://doi.org/10.1175/1520-0450(2000)039<1514:SAOPVA>2.0.CO;2).